A&A manuscript no.
(will be inserted by hand later)

Your thesaurus codes are:
03(11.01.2; 11.19.1; 11.09.1 NGC 7582)

ASTRONOMY AND ASTROPHYSICS

arXiv:astro-ph/9906444v1 28 Jun 1999

The 10-200 μm spectral energy distribution of the prototype Narrow-Line X-ray galaxy NGC 7582 ⋆

Mario Radovich[1], **Ulrich Klaas**[1], **José Acosta-Pulido**[2] **and Dietrich Lemke**[1]

[1] Max-Planck-Institut für Astronomie, Königstuhl 17, D-69117 Heidelberg, Germany

[2] Instituto de Astrofisica de Canarias, E-38200 La Laguna, Tenerife, Spain

Received 16 March 1999 /Accepted 7 June 1999

Abstract. We present the spectral energy distribution (SED) between 10 and 200 μm obtained for the prototype Narrow-Line X-Ray Galaxy NGC 7582 with ISOPHOT, the photometer on board the *Infrared Space Observatory*. The emission is spatially extended and we separated for the first time the nuclear and extranuclear infrared SEDs. The nuclear luminosity ($L_{IR} \sim 4.5\times10^{10}\ L_\odot$) is dominated by cold ($T \sim 32$ K) dust emission mainly due to star formation activity; warm ($T \sim 122$ K) dust emission is also present and is probably related to the active nucleus. In addition to a cold component of 30 K, the extranuclear SED ($L_{IR} \sim 1.7\times10^{10}\ L_\odot$) shows emission by colder ($T \sim 17$ K) dust: this very cold component comprises 90% of the total dust mass of $9.8\times10^7\ M_\odot$.

Key words: galaxies: Seyfert – galaxies: individual: NGC 7582

1. Introduction

NGC 7582 (z=0.00525) is a highly inclined ($i \sim 60°$) barred spiral galaxy; its blue luminosity corrected for galactic and internal extinction is $\sim 3.5\times10^{10}$ $L_\odot$ (Claussen & Sahai 1992) with a Hubble constant $H_0 = 75$ km s^{-1} Mpc^{-1}. It was classified by Mushotzky (1982) as a Narrow-Line X-ray Galaxy (NLXG) due to its high X-ray luminosity, L(2-10 keV) $\sim 7\times10^8$ $L_\odot$, typical of low-luminosity Seyfert 1 galaxies, but with narrow (FWHM $<$ 200 km s^{-1}) emission lines, more typical of Seyfert 2 or starburst galaxies.

Recent ASCA observations (Schachter et al. 1998, Xue et al. 1998) revealed high variability on short (~ 5.5 hours) time scales in the hard X-ray range (2-10 keV), typical of an AGN; in particular, Schachter et al. (1998) report a hard X-ray flux drop by 40% in ~ 6 ks, implying a source size of $\sim 2\times10^{14}$ cm. In addition, the existence of an active nucleus is suggested by the detection of an ionization cone in [O III] λ5007 narrow–band images (Storchi-Bergmann & Bonatto 1991) and by the presence of high ionization emission lines (e.g. [Ne V] λ3426). Genzel et al. (1998) report the detection of both high-ionization (e.g. [O IV] λ25.9μm, [N V] λ14.3μm) and low–ionization (e.g. [Ne II] λ12.8μm, [S III] λ18μm) emission lines with the ISO short-wavelength grating spectrometer (SWS). The low-ionization lines may be produced either by a starburst or by an AGN (Radovich et al. 1998). A composite model, where high-ionization lines are produced in gas ionized by the AGN and the low-ionization lines are enhanced in

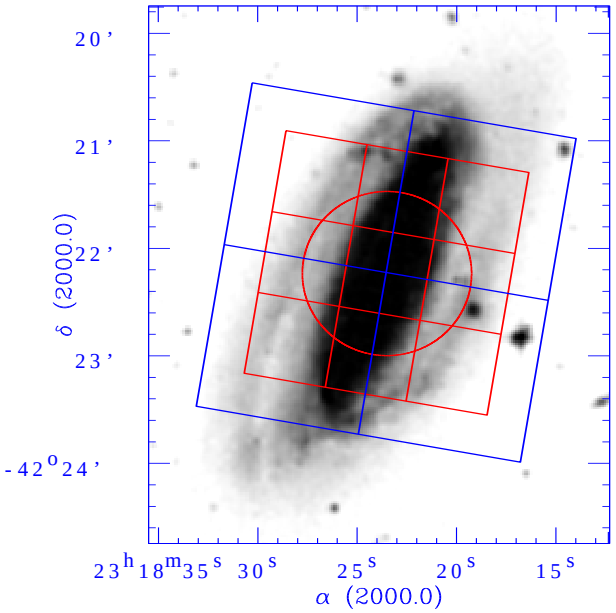

Fig. 1. The positions of the circular PHT-P aperture and of the C100 (3x3) and C200 (2x2) arrays are overplotted on a J-band image of NGC 7582 obtained from the SkyView survey analysis system.

Send offprint requests to: M. Radovich (radovich@mpia-hd.mpg.de)

⋆ Based on observations with ISO, an ESA project with instruments funded by ESA Member States (especially the Principal Investigator countries: France, Germany, Netherlands and the United Kingdom) and with the participation of ISAS and NASA.

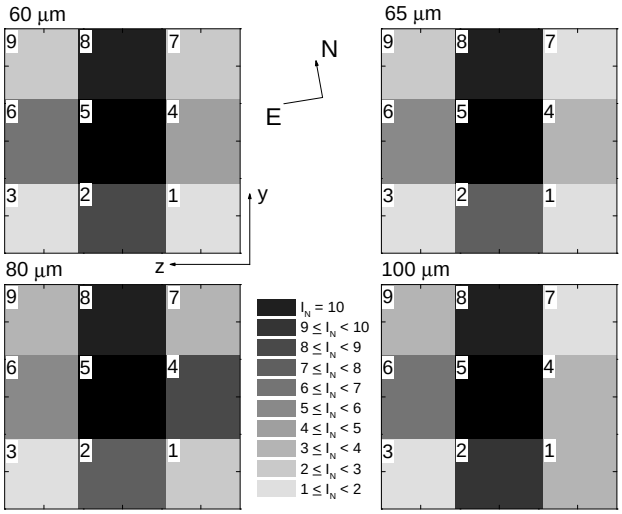

Fig. 2. Intensity distribution in the C100 array after background subtraction. Intensities in the border pixels have been normalized to the range 1-10, with darker colours indicating increasing intensities; the intensity in the central pixel is outside the scale.

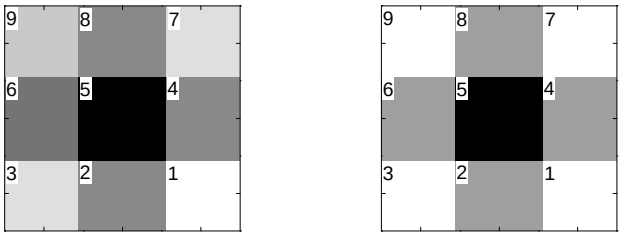

Fig. 3. Intensity distribution produced by a pointlike source in the C100 array. The intensity in the central pixel and the intensity scale are the same as those in the 60μm filter for NGC 7582, displayed in Fig. 2. *Left:* observations of the star HR 5340; *right:* theoretical monochromatic footprint as given in Table 2.

starburst regions, is also possible and would explain the [O III] λ5007/Hβ ratio of $\sim$ 3 (Storchi-Bergmann et al. 1995), lower than usually observed in AGNs. According to the 'unified model' (Antonucci 1993), broad emission lines are extinguished in Seyfert 2 galaxies by a dusty torus located at $\leq$ 100 pc from the nucleus, but they should be scattered into our line of sight by free electrons around the torus and should be observed in polarized light. However, Heisler et al. (1997) did not detect broad emission lines in the polarized spectrum of NGC 7582: they attributed the non-detection of polarized broad lines to the fact that our line of sight passes through an amount of dust in the torus which is larger than in Seyfert 2s with polarized broad lines.

The presence of strong star formation activity in the central kpc was concluded from other indicators. Morris et al. (1985) showed that in the inner kpc the Hα emission suggests a rotating disk of HII regions in the plane of the galaxy. Recently Aretxaga et al. (1999) reported the appearance of broad (FWHM $\sim$ 10000 km s^{-1}) permitted lines in the period July - October 1998: they explained it as the result of supernova explosions in the circumnuclear starburst, rather than as a change of the reddening in the torus which would allow to see the inner nuclear regions. The non-thermal radio emission probably originates in many supernova remnants associated with this starburst, as found by Forbes & Norris (1998). In the infrared, the 8-13 μm emission is characterized by the presence of polycyclic aromatic hydrocarbon (PAH) features as revealed by ground-based (Frogel et al. 1982, Roche et al. 1984) and, more recently, by ISO SWS observations (Genzel et al. 1998). Their strength is much more typical of starbursts rather than of AGNs: in fact, Genzel et al. (1998) found that the typical strength of the 7.7μm PAH feature, defined in their Table 1, is 0.04 in AGNs and 3.6 in starbursts; they find a value of 2.5 in NGC 7582. Multi-aperture observations performed by Frogel et al. (1982) showed that the 10 μm emission comes from a region smaller than 8″, but its origin is still unclear. Using the FIR to X-ray luminosity correlation for normal and starburst galaxies, Turner et al. (1997) found that the maximum contribution of a starburst to the 0.5-4.5 keV emission is $\sim$ 34%. According to Xue et al. (1998), the soft X-ray emission (0.5 - 2 keV) is the sum of scattered emission from the nucleus and emission from the starburst, the latter being $\sim$ 10-20%. In their Hubble Space Telescope imaging survey of nearby AGNs, Malkan et al. (1998) detected dust lanes running across the nucleus of NGC 7582, at a distance of some hundreds of parsecs: this dust component external to the torus may contribute to obliterate the broad polarized lines whereas the scattered X-ray photons may still be observed.

There is therefore strong evidence that NGC 7582 contains a 'buried' AGN with the active nucleus residing in a dusty environment and coexisting with a circumnuclear starburst. Schachter et al. (1998) suggested that all NLXGs are obscured AGNs. Because of its prototype nature and brightness we observed the infrared SED of this object with ISO (Kessler et al. 1996) to determine the relative contribution of the various components to the total energy budget.

Table 1. Pointing of the observations. The on-position was centered on the object, the off-position was used for background subtraction.

Name	Date	RA (2000)	DEC (2000)
NGC 7582 on	24 Dec 97	$23^h18^m23^s.5$	-42°22′14″
NGC 7582 off	24 Dec 97	$23^h17^m55^s.1$	-42°20′41″

Table 2. Footprint values adopted for the spatial decomposition of C100 (Herbstmeier, private communication) and C200 (Klaas et al., in preparation) data. For C100 these are calculated values from a convolution of the monochromatic point spread function with the C100 pixel field size. For C200 they are empirically derived from a comparison of measurements of point sources centered on the arrays with raster measurements centered on each pixel.

C100 Detector				
Pixel	60μm	65μm	80μm	100μm
1	0.0087	0.0132	0.0178	0.0228
2	0.0429	0.0423	0.0379	0.0385
3	0.0087	0.0123	0.0176	0.0228
4	0.0440	0.0434	0.0377	0.0382
5	0.6625	0.6587	0.6416	0.5561
6	0.0440	0.0434	0.0377	0.0382
7	0.0087	0.0123	0.0176	0.0228
8	0.0429	0.0423	0.0379	0.0385
9	0.0087	0.0132	0.0178	0.0228
C200 Detector				
Pixel	120μm	150μm	180μm	200μm
1-4	0.1435	0.1670	0.1875	0.1875

2. Observations and Data Reduction

NGC 7582 was observed with ISOPHOT (Lemke et al. 1996) in staring mode with the multi-filter AOTs (Astronomical Observation Templates) PHT03 (PHT-P) and PHT22 (PHT-C) (Klaas et al. 1994) on the target and on one off-position (Table 1). The aperture size used with PHT-P was 99″. On-source integration times were 64s with PHT-P and 32s with PHT-C; the same times were used for the off-source measurement. The data reduction was performed using the ISOPHOT Interactive Analysis tool (PIA, version 7.2) together with the calibration data set V 4.0 (Laureijs et al. 1998): corrections were made for non-linearity effects of the electronics, disturbancies by cosmic rays (deglitching) and signal dependence on the reset interval time. The flux calibration is based on measurements with the thermal fine calibration sources (FCS) on board. There was one FCS measurement per detector in the 12 μm, 25 μm, 100 μm and 150 μm filters . The photometric accuracies for this observing mode and brightness range are $\sim$ 10% in the absolute calibration (FCS in the same filter) and $\leq$ 30% in the relative calibration (no FCS in this filter), see Klaas et al. (1998).

3. Results and Discussion

3.1. Spatial decomposition

The redshift of NGC 7582 gives a projected linear scale of 102 pc/arcsec. The diameter at the 25 mag arcsec^{-2} blue isophote is 5′ (De Vaucouleurs et al. 1991), which is larger than both the C100 and C200 detectors ($\sim$ 2.′2 and 3′, respectively, see Fig. 1). Indeed, a first hint that infrared emission is extended was found by Sanders et al. (1995) in the IRAS Bright Galaxy Sample data reprocessed using the HIRES algorithm. They report extended emission in NGC 7582 at 12 and 25 μm (size $>$ 0.′75) and 60 μm (size $>$ 1.′75), but could not resolve it at 100 μm (size $<$ 2.′8). The intensity distribution in the C100 array after background subtraction is displayed in Fig. 2. For comparison we show in Fig. 3 the patterns expected from a pointlike source. The *left* pattern is that *observed* for a star, the *right* pattern was *generated* using the calculated monochromatic footprint values of Table 2; in both cases the intensity in the central pixel was matched to that found in NGC 7582 (60μm filter). The two distributions are slightly different since the observed one includes effects by small telescope pointing offsets and chromatic effects within the width of the bandpass of the 60μm filter. It can be seen that the intensity distribution in NGC 7582 is not that expected from a pointlike source. Pixels 2 and 8, which are aligned along the major axis of the galaxy, clearly show an excess emission; the values in the other border pixels are closer to those given by the intensity distribution of a pointlike source.

In order to disentangle the extended and pointlike components, we proceeded as follows. We assumed that (*i*) the emission is composed of a compact central source plus extended emission and (*ii*) the array is centered on the compact source. The total intensity observed in each pixel is then given by:

$$I_{\rm i} = f_{\rm i} I_{\rm nuc} + I_{\rm e,i}, \quad (1)$$

where $f_{\rm i}$ is the fraction of the intensity from the pointlike source falling on each pixel (Table 2); $I_{\rm nuc}$ is the intensity emitted by the pointlike *nuclear* source, $I_{\rm e,i}$ is the extended emission from the extranuclear regions detected by each pixel. The total extranuclear emission is defined as $I_{\rm e} = \sum_{i=1}^{\rm np} I_{\rm e,i}$ (C100: np=9, C200: np=4): we shall call it the *disk* emission hereafter. For C100 we made the further assumption that $I_{\rm e,5}$ is the same as in pixels 2 and 8, $I_{\rm e,5} = (I_{\rm e,2} + I_{\rm e,8})/2$; this seems plausible from the observed intensity distribution on the array (Fig. 2).

For C200 this approach was not feasible due to the lack of a central pixel: we extrapolated the nuclear flux ($I^*_{\rm nuc}$) from the blackbody fit of the decomposed nuclear C100 values. The extranuclear component was then obtained using Eq. 1 with the footprint scaling for C200 (Table 2):

$$I_{\rm e,i} = I_{\rm i} - f_{\rm i} I^*_{\rm nuc}. \quad (2)$$

An estimate of the uncertainties introduced by this procedure was computed by propagating the statistical uncertainty of the intensities in each pixel, which is typically $\Delta I_{\rm i}/I_{\rm i} < 5\%$ (Laurejis & Klaas 1999). The comparison (see Table 3) with the photometric accuracies quoted in Sect. 2 shows however, that the final uncertainties are

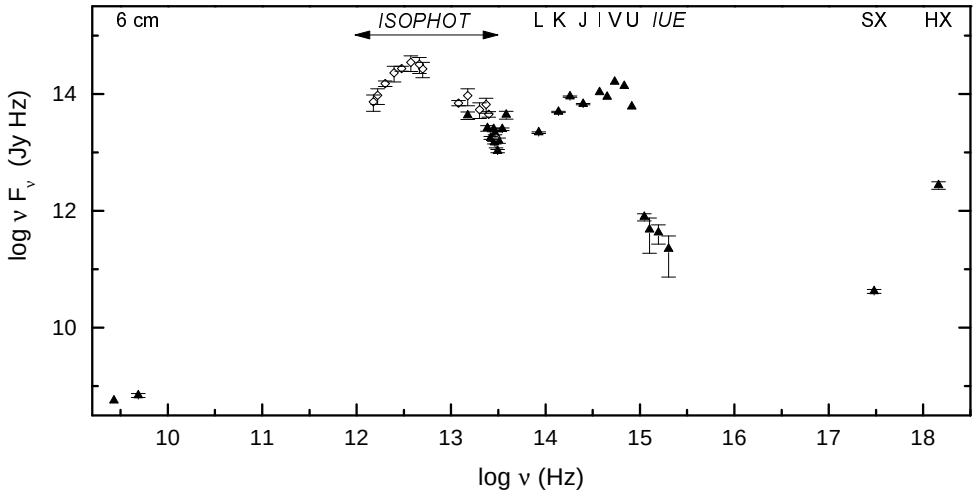

Fig. 4. The radio to X-ray spectral energy distribution of NGC 7582. Diamonds: ISOPHOT data (nucleus+disk); triangles: photometric data from the NASA-IPAC extragalactic database (NED), the SX (0.5-2 keV) and HX (2-10 keV) fluxes are from Xue et al. (1998). Uncertainties are plotted if available.

dominated by systematic errors in background subtraction and relative filter-to-filter calibration which affect the total measurement, rather than the individual pixel measurements.

3.2. Spectral Energy Distribution

In Fig. 4 we show the SED of NGC 7582 from the radio to X–ray frequencies, including the new ISOPHOT data points. The radio to near-IR SEDs are similar in Seyfert and starburst galaxies (Schmitt et al. 1997). The peak of the SED is located in the far-infrared and is likely due to the dust heated by the starburst. The rise in the blue wavelengths of the visual range can be either due to the AGN or to the starburst. Schmitt et al. (1999) found that nearly 50% of the flux at λ5870 Å is produced by a population of stars with an age $\leq$ 100 Myr, and that the contribution from the nuclear featureless continuum is only $\leq$ 5%; the remaining 45% comes from stars older than 1 Gyr. The ultraviolet emission was detected by IUE in a $10'' \times 20''$ aperture (linear projected size of 1 kpc $\times$2 kpc). Heckman et al. (1995) suggested that the steep ultraviolet continuum, $f_\lambda \propto \lambda^{1.7}$, may be produced by a very dusty starburst. This was later confirmed by Bonatto et al. (1998), who reproduced the ultraviolet continuum of a sample of nearby spiral galaxies by stellar population synthesis and concluded that in the case of NGC 7582 the UV light is dominated by recent star formation with an age $t \leq 500$ Myr in a reddened nuclear starburst. The presence of the active nucleus becomes evident only in the hard X–ray domain.

The ISOPHOT spectral energy distribution and its decomposition into several spatial and temperature components is presented in Fig. 5. We fitted them with a modified blackbody, i.e. a blackbody with a wavelength dependent emissivity (see e.g. Hildebrand 1983); we adopted an emissivity $\propto \lambda^{-2}$. Colour correction was performed in an iterative way, namely a first value of the temperature was adopted and the corresponding colour correction factors applied: the resulting SED was fitted with modified blackbodies using a non-linear least squares algorithm giving new values of the temperature. The whole procedure was then repeated until convergence. The fluxes derived are listed in Table 3, the temperature components are given in Table 4. The fluxes measured in the PHT-P filters ($\leq$ 25 μm) with the $99''$ aperture are in good agreement with the values of ground-based observations (Roche et al. 1984) with smaller apertures ($8''$): we therefore conclude that an extranuclear component is negligible. The 12 and 25 μm ISO fluxes are also in good agreement with the peak IRAS intensities given by Sanders et al. (1995) with an angular resolution (width at 25% peak intensity $\sim 94''$ and $70''$, respectively) comparable to that of the PHT-P aperture.

The results of the decomposition of the nuclear and disk SEDs are:

1. *Nucleus* – The SED between 10 and 25μm (PHT-P) is well fitted by a warm ($T = 122$ K) component which is typical of Seyfert galaxies (Pérez García et al. 1998), where dust in the torus is heated by the active nucleus. The deviations of the measured data from the fit are within the general calibration accuracy, $\Delta \leq 15\%$, with the exception of the 12.8 μm and 15 μm values ($\Delta \sim$ 30%). The contribution of the [Ne II] λ12.8 μm line cannot account for the excess in the 12.8 μm band: in fact the intensity given by Genzel et al. (1998) amounts only to $\sim$ 3% of the integrated flux in this band. At $\lambda > 60\mu$m (C100) we see a well defined cold (T $\sim$ 32 K) component. Since we have $S_\nu(25)/S_\nu(60) = 0.13$,

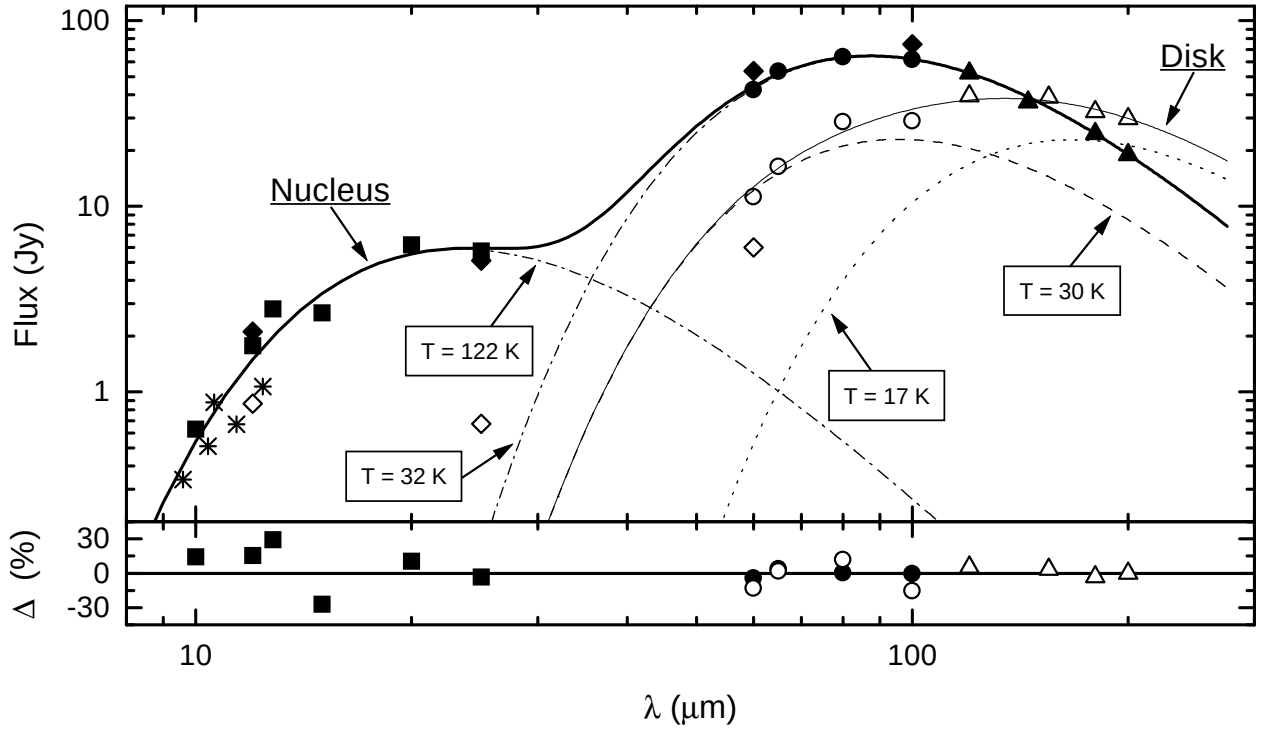

Fig. 5. Decomposition of the SED of NGC 7582. Filled symbols: nuclear fluxes; open symbols: disk fluxes. Squares: PHT-P; circles: C100; triangles: C200 (the 150 μm disk and nuclear points have been slightly shifted in wavelength to avoid overlapping). Diamonds: IRAS data from Sanders et al. (1995). Asterisks: ground-based observations from Roche et al. (1984). The black body fits are indicated as follows. Nucleus: dashed-dotted lines (PHT-P and PHT-C components); the thick line gives the sum of the two components. Disk: dashed (C100) and dotted (C200) line; the thin line shows the sum of the two components. The lower panel displays the deviation of the measured ISOPHOT photometric data from the fit.

whereas in Seyfert galaxies $S_\nu(25)/S_\nu(60) > 0.2$ (Miley et al. 1985), we conclude that at these wavelengths the emission is dominated by dust heated by the starburst. According to the colour-colour diagrams by Dopita et al. (1998), the FIR colours of NGC 7582 may be interpreted as the composition of substantial circumnuclear star formation emission plus emission from an active nucleus observed through a dusty environment ($\tau_{12\mu m} > 3$): the dust may be located both in the accretion torus and in the circumnuclear starburst.

2. *Disk* – The signal in C100 is dominated by a component whose temperature (T $\sim$ 30 K) is similar to that found in the nucleus. The signal in C200 reveals a colder component, T $\sim$ 17 K; due to absence of data points longward of 200 μm, the fit is not very well constrained and has an uncertainty $\Delta T \sim 3$ K. This temperature is typical of dust heated by the interstellar radiation field; the presence of very cold dust which dominates the emission in the outer regions of the disk has also been found in the analysis of ISOPHOT data both for active (Pérez García et al. 1998) and normal (Krügel et al. 1998, Alton et al. 1998) galaxies.

3.3. Luminosities and dust masses

Luminosities between 1 and 1000 μm derived for the different components are compiled in Table 4. The ratio of the nuclear starburst to disk luminosity is 2^{+2}_{-1}. Rowan-Robinson & Crawford (1989) obtained a value of 2.1 fitting the IRAS values with starburst and disk emission models: this provides a reliability check for the decomposition based on the spatial resolution we obtained.

The spatial and spectral decomposition allows an estimate which is more reliable than with IRAS of the star formation rates and dust masses (Table 4). Star formation rates were derived for the cold (30 K) nuclear and disk components only, according to Kennicutt (1998); dust masses were computed according to Klaas & Elsässer (1993), assuming dust grain properties as in Hildebrand (1983) for the emissivity adopted here ($\propto \lambda^{-2}$):

$$SFR = 1.7 \times 10^{-10} L_{\rm IR}/L_\odot \quad [M_\odot \ {\rm yr}^{-1}], \tag{3}$$

$$M_{\rm d} = 7.9 \times 10^{-5} (T_{\rm K}/40)^{-6} \ L_{\rm IR}/L_\odot \quad [M_\odot]. \tag{4}$$

The nuclear star formation rate of $\sim 6 M_\odot$ yr^{-1} is typical of bright IR galaxies (Kennicutt 1998), and confirms the presence of a moderate star formation activity in the

Table 3. Central wavelengths and spectral resolutions of the ISOPHOT filter bands, total fluxes (not colour corrected) and fluxes obtained after separation of the nuclear and disk components, blackbody fitting and colour correction; statistical uncertainties for the decomposed components (in italics) and photometric accuracies are also given. We show for comparison the IRAS fluxes from Sanders et al. (1995); a proper colour correction is applied only to the peak and extended values. Fluxes and uncertainties are in Jy.

		ISOPHOT								IRAS			
λ_c	$\frac{\lambda_c}{\Delta\lambda_c}$	Total	phot	Nucleus	*stat*	phot	Disk	*stat*	phot	Total		Peak	Extended
P1 Detector													
10	5.6	0.6	±0.2	0.6		±0.2							
12	5.6	1.5	±0.2	1.8		±0.2				2.3	±0.1	2.1	0.9
12.8	5.3	2.8	±0.8	2.8		±0.8							
15	1.8	2.6	±0.8	2.7		±0.8							
P2 Detector													
20	2.3	6	±2	6		±2							
25	2.6	7.2	±0.7	5.8		±0.6				7.5	±0.4	5.1	0.7
C100 Detector													
60	2.5	57	±17	42	± *2*	±13	11	±*1*	±3	52	±3	54	6
65	1.1	59	±18	53	± *3*	±16	16	±*1*	±5				
80	1.7	81	±24	64	±*4*	±19	28	±*2*	±9				
100	2.2	85	±9	62	±*4*	±6	29	±*2*	±3	78	±5		
C200 Detector													
120	2.4	90	±27	52	±*3*	±16	39	±*4*	±12				
150	1.9	75	±8	36	±*2*	±4	39	±*4*	±4				
180	2.6	59	±18	25	±*1*	±7	32	±*3*	±10				
200	3.6	50	±15	19	±*1*	±6	30	±*2*	±9				

Table 4. Aperture diameters and derived projected linear sizes (radii), infrared luminosities, dust masses and star formation rates derived for the different components; uncertainties given by the blackbody fit are displayed.

Aperture [″]	Radius [kpc]	T [K]	L(1-1000 μm) [$L_\odot$]	M_{dust} [$M_\odot$]	SFR [$M_\odot$ yr^{-1}]
Nucleus					
99	< 5	122±5	$(12^{+5}_{-4}) \times 10^9$	$(11^{+2}_{-1}) \times 10^2$	–
43	< 2	32±0.3	$(33^{+4}_{-4}) \times 10^9$	$(93^{+5}_{-5}) \times 10^5$	$5.8^{+0.7}_{-0.6}$
Disk					
138	≤ 7	30±2	$(11^{+8}_{-5}) \times 10^9$	$(5^{+1}_{-1}) \times 10^6$	2^{+1}_{-1}
182	≤ 9	17±3	$(6^{+10}_{-5}) \times 10^9$	$(8^{+2}_{-2}) \times 10^7$	–

inner kpc. A lower star formation rate, $\sim 2 M_\odot$ yr^{-1}, is derived for the disk.

According to Claussen & Sahai (1992) the atomic and molecular hydrogen masses in NGC 7582 are M(HI) = 4.3×10^9 M$_\odot$ and M(H$_2$) = 4.4×10^9 M$_\odot$, respectively. The dust to gas mass ratio would be $\sim 1/600$, if we considered only the warm and cold components (nucleus + disk) detected by C100; this would give a dust mass $M_d \sim 1.4\times10^7$ M$_\odot$. The addition of the 17 K component revealed by C200 increases the dust mass by a factor of 7; the dust mass is now $M_d \sim 9.8 \times 10^7$ M$_\odot$, the dust to gas mass ratio is 1/90, close to the canonical value. It should be noted that due to the strong dependence of the dust mass on the temperature, the $\Delta T = 3$ K uncertainty may change the dust mass of the very cold component by a factor of 3. A more detailed error calculation shows however that the final uncertainty on the dust mass is much lower (see Table 4). The dust mass of the nuclear warm component, probably associated with the torus, is $M_d \sim 3 \times 10^3$ M$_\odot$.

4. Summary

We obtained ISOPHOT data for the prototype NLXG NGC 7582 from 10 to 200 μm and found that its emission is extended in the 60 to 200 μm range along the major axis of the galaxy. We performed a spatial decomposition into a nuclear and a disk component. The SED in the nucleus (r < 2 kpc) amounts to 70% of the total IR luminosity of 6×10^{10} $L_\odot$; it was decomposed into a warm (122 K) component, probably related to dust heated by the active nucleus, and a cold (32 K) component coming from a circumnuclear starburst. The IR colours are consistent with the values expected for an obscured active nucleus

plus circumnuclear star formation. We conclude that the most likely interpretation of the NLXG nature of NGC 7582 is that the high X–ray luminosity is produced by the active nucleus, which is obscured at longer wavelengths by dust located in the circumnuclear regions; the heating of the dust by the starburst produces the far-infrared emission. The availability of the data longward of 100 μm allowed the detection of a very cold (17 K) component in the SED of the disk. This very cold component is due to dust heated by the interstellar radiation field and it dominates the dust mass of the galaxy; its inclusion increases the dust mass detected now by a factor of 7.

Acknowledgements. The ISOPHOT consortium is headed by the Max-Planck-Institut für Astronomie, Heidelberg, Germany. The ISOPHOT development and the postoperational phase of the ISOPHOT Data Centre of MPIA Heidelberg are funded by Deutsches Zentrum für Luft- und Raumfahrt (DLR), Bonn. PIA has been jointly developed by the ESA Astrophysics Division and the ISOPHOT consortium. This research has made use of the NASA-IPAC extragalactic database (NED) which is operated by the Jet Propulsion Laboratory, Caltech, under contract with the NASA. We thank the anonymous referees for their comments which improved this paper.

References

Alton P.B., Trewhella M., Davies J.I., et al. 1998, A&A 335, 807
Antonucci R., 1993, ARA&A 31, 473
Aretxaga I., Joguet B., Kunth D., et al. 1999, ApJL, in press
Bonatto C., Pastoriza M.G., Alloin D., Bica E. 1998, A&A 334, 439
Claussen M.J., Sahai R. 1992, AJ 103, 1134 (Luminosities were derived assuming a Hubble constant of 50 km s^{-1} Mpc^{-1}).
de Vaucouleurs G., de Vaucouleurs A., Corwin H.G., et al. 1991, Third Reference Catalogue of Bright Galaxies (ed. Springer Verlag)
Dopita M.A., Heisler C., Lumsden S., Bailey J. 1998, ApJ 498, 570
Forbes D.A., Norris R.P. 1998, MNRAS 300, 757
Frogel J.F., Elias J.H., Phillips M.M. 1982, ApJ 260, 70
Genzel R., Lutz D., Sturm E., et al. 1998, ApJ 498, 579
Heckman T.M., Krolik J., Meurer G., et al. 1995, ApJ 452, 549
Heisler C.A., Lumsden S.L., Bailey J.A. 1997, Nat 385, 700
Hildebrand R.H. 1983, N83 24436
Kennicutt R.C. 1998, ARA&A 36, 189
Kessler M.F., Steinz J.A., Anderegg M.E., et al. 1996, A&A 315, L27
Klaas U., Elsässer H. 1993, A&A 280, 76
Klaas U., Krüger H., Heinrichsen I., et al. 1994, ISOPHOT Observer's Manual, Version 3.1 (Noordwijk: ESA), ISO Explanatory Library, http://www.iso.vilspa.esa.es/manuals/iso_pht/om311.html
Klaas U., Laurejis R.J., Radovich M., Schulz B. 1998, ISOPHOT Calibration Accuracies, Version 2.0, ISO Explanatory Library, SAI/98-049/Rp, http://www.iso.vilspa.esa.es/manuals/PHT/accuracies/pht_accuracies20/
Krügel E., Siebenmorgen R., Zota V., Chini R. 1998, A&A 331L, 9
Laureijs R.J., Klaas U. 1999, ISOPHOT Error Budgets V 1.0, SAI/98-091/Dc, http://www.iso.vilspa.esa.es/ manuals/PHT/error_budget/
Laureijs R.J., Klaas U., Richards P., Schulz B. 1998, ISOPHOT Data Users Manual, V 4.0, ISO Explanatory Library, SAI/95-220/Dc, http://www.iso.vilspa.esa.es/manuals/pht_idum4/
Lemke D., Klaas U., Abolins J., et al. 1996, A&A 315, L64
Malkan A.M., Gorjian V., Tam R. 1998, ApJ 117, 25
Miley G.K., Neugebauer G., Soifer B.T. 1985, ApJ 193, L11
Morris S., Ward M., Whittle M., Wilson A.S., Taylor K. 1985, MNRAS 216, 193
Mushotzky R.F. 1982, ApJ 256, 92
Pérez García A.M., Rodríguez Espinosa J.M., Santolaya Rey A.E. 1998, ApJ 500, 685
Radovich M., Hasinger G., Rafanelli P. 1998, Astron. Nachr. 319, 325
Roche P.F., Aitken D.K., Phillips M.M., Whitmore B. 1984, MNRAS 207, 35
Rowan-Robinson M., Crawford J. 1989, MNRAS 238, 523
Sanders D.B., Egami E., Lipari S., et al. 1995, AJ 110, 1993
Schachter J.F., Fiore F., Elvis M., et al. 1998, ApJ 503, L123
Schmitt H.R., Kinney A.L., Calzetti D., Storchi Bergmann T. 1997, AJ 114, 592
Schmitt H.R., Storchi-Bergmann T., Cid Fernandes R. 1999, MNRAS 303, 173
Storchi-Bergmann T., Bonatto C. 1991, MNRAS 250, 138
Storchi-Bergmann T., Kinney A.L., Challis P. 1995, ApJS 98, 103
Turner T.J., George I.M., Nandra K., Mushotzky R.F. 1997, ApJS 113, 23
Xue S.J., Otani C., Mihara T., Cappi M., Matsuoka M. 1998, PASJ 50, 519